Mon. Not. R. Astron. Soc. **000**, 1–?? (2011) Printed 8 December 2011 (MN LATEX style file v2.2)

Search for cold gas in $z > 2$ damped Lyα systems: 21-cm and H_2 absorption

R. Srianand[1⋆], N. Gupta[2], P. Petitjean[3], P. Noterdaeme[3], C. Ledoux[4], C. J. Salter[5] and D. J. Saikia[6]

[1] *IUCAA, Ganeshkhind, Pune 411007, India*
[2] *Netherlands Institute for Radio Astronomy (ASTRON), Postbus 2, 7990 AA, Dwingeloo, The Netherlands*
[3] *Université Paris 6, UMR 7095, Institut d'Astrophysique de Paris-CNRS, 98bis Boulevard Arago, 75014 Paris, France*
[4] *European Southern Observatory, Alonso de Córdova 3107, Casilla 19001, Vitacura, Santiago 19, Chile*
[5] *Arecibo Observatory, NAIC, HC3 Box 53995, Arecibo, Puerto Rico, PR 00612, USA*
[6] *NCRA-TIFR, Ganeshkhind, Pune 411007, India*

Accepted. Received; in original form

ABSTRACT

We present the results of a systematic Green Bank Telescope (GBT) and Giant Metrewave Radio Telescope (GMRT) survey for 21-cm absorption in a sample of 10 damped Lyman-α (DLA) systems at $2 \leq z_{\rm abs} \leq 3.4$. Analysis of L-band Very Long Baseline Array (VLBA) images of the background QSOs are also presented. We detect 21-cm absorption in only one DLA (at $z_{\rm abs} = 3.1745$ towards J1337+3152). Thus the detection rate of 21-cm absorption is $\sim 10\%$ when no limit on the integrated optical depth ($\int \tau(v)dv$) is imposed and $\sim 13\%$ for a 3σ limit of 0.4 km s^{-1}. Combining our data with the data from the literature (a sample of 28 DLAs) and assuming the measured core fraction at milliarcsecond scale to represent the gas covering factor, we find that the H I gas in DLAs at $z \geq 2$ is predominantly constituted by warm neutral medium. The detection rate of 21-cm absorption seems to be higher for systems with higher N(H I) or metallicity. However, no clear correlation is found between the integrated 21-cm optical depth (or the spin-temperature, $T_{\rm S}$) and either N(H I), metallicity or velocity spread of the low ionization species. There are 13 DLAs in our sample for which high resolution optical spectra covering the expected wavelength range of H_2 absorption are available. We report the detection of H_2 molecules in the $z_{\rm abs} = 3.3871$ 21-cm absorber towards J0203+1134 (PKS 0201+113). In 8 cases, neither H_2 (with molecular fraction $f(H_2) \leq 10^{-6}$) nor 21-cm absorption (with $T_{\rm S}/f_{\rm c} \geq 700$ K) are detected. The lack of 21-cm and H_2 absorption in these systems can be explained if most of the H I in these DLAs originate from low density high temperature gas. In one case we have a DLA with 21-cm absorption not showing H_2 absorption. In two cases, both species are detected but do not originate from the same velocity component. In the remaining 2 cases 21-cm absorption is not detected despite the presence of H_2 with evidence for the presence of cold gas. All this is consistent with the idea that the H_2 components seen in DLAs are compact (with sizes of ≤ 15 pc) and contain only a small fraction (i.e typically $\leq 10\%$) of the total N(H I) measured in the DLAs. This implies that the molecular fractions $f(H_2)$ reported from the H_2 surveys should be considered as conservative lower limits for the H_2 components.

Key words: quasars: active – quasars: absorption lines – galaxies: ISM

1 INTRODUCTION

The Galactic interstellar medium (ISM) has a multiphase structure with neutral hydrogen being distributed between the cold neutral (CNM), warm neutral (WNM) and warm ionized (WIM) media. A large fraction of the gas is also found in diffuse, translucent and dense molecular clouds. Newly formed stars are associated with these dense molecular clouds and strongly influence the physical state of the rest of the gas in different forms through radiative and mechanical inputs. The physical conditions in the multiphase ISM depend on the UV background radiation field, metallic-

⋆ E-mail:anand@iucaa.ernet.in

ities, dust content and the density of cosmic rays (see Figs. 5, 6 and 7 in Wolfire et al. 1995). In addition, the filling factor of the different phases depends sensitively on the supernova rate (de Avillez & Breitschwerdt 2004). Therefore, detecting and studying the multiphase ISM in external galaxies has great importance for our understanding of galaxy evolution.

Damped Lyman-α systems (DLAs) are the highest H I column density absorbers seen in QSO spectra, with N(H I)$\geq 2 \times 10^{20}$ cm^{-2}. These absorbers trace the bulk of the neutral hydrogen at $2 \leq z \leq 3$ (Prochaska et al. 2005; Noterdaeme et al. 2009) and have long been identified as revealing the interstellar medium of the high-redshift precursors of present day galaxies (for a review see, Wolfe et al. 2005).

The typical dust-to-gas ratio of DLAs, is less than one tenth of that observed in the local ISM, and only a small fraction ($< 10\%$) of DLAs show detectable amounts of molecular hydrogen (Petitjean et al. 2000; Ledoux et al. 2003; Noterdaeme et al. 2008) with the detection rate being correlated to the dust content of the gas (Petitjean et al. 2006). The estimated temperature and molecular fraction in these systems are consistent with them originating from the CNM (Srianand et al. 2005). It has been shown recently that strong C I absorbers detected in low-resolution Sloan Digital Sky Survey (SDSS) spectra are good candidates for H_2 bearing systems. Indeed these absorbers have yielded the first detections of CO molecules in high-z DLAs (Srianand et al. 2008; Noterdaeme et al. 2009, 2010, 2011). The properties of these absorbers are similar to those of translucent molecular clouds. The fact that no DLA is found to be associated with a dense molecular cloud, a fundamental ingredient of star-formation, is most certainly related to the large extinction that these clouds are expected to produce and/or the small size of such regions (Zwaan & Prochaska 2006) making detections difficult.

Thus, most DLAs detected in optical spectroscopic surveys seem to probe the diffuse H I gas (Petitjean et al. 2000). However, about 50% of the DLAs show detectable C II* absorption (Wolfe et al. 2008), and Wolfe et al. (2003) argued that a considerable fraction of the C II* absorption in DLAs originates from CNM gas (see however Srianand et al. 2005). Detection of 21-cm absorption is the best way to estimate the CNM fraction of DLAs as it is sensitive to both N(H I) and thermal state of the gas (Kulkarni & Heiles 1988). This is why it is important to search for 21-cm absorption in DLAs over a wide redshift range. While a good fraction of DLAs/sub-DLAs preselected through Mg II absorption seems to show 21-cm absorption at $z \sim 1.3$ (see for example Gupta et al. 2009; Kanekar et al. 2009), searches for 21-cm absorption in DLAs at $z_{\rm abs} \geq 2$ have mostly resulted in null detections (see Kanekar & Chengalur 2003; Curran et al. 2010) with only four detections reported till now (see Wolfe et al. 1985; Kanekar et al. 2006, 2007; York et al. 2007). The low detection rate of 21-cm absorption in high-z DLAs can be related to either the gas being warm (i.e high spin temperature, $T_{\rm S}$, as suggested by Kanekar & Chengalur (2003)) and/or the low value of covering factor (f_c) through high-z geometric effects (Curran & Webb 2006).

The best way to address the covering factor issue is to perform milliarcsecond scale spectroscopy in the redshifted 21-cm line using very long baseline interferometry (VLBI) to measure the extent of absorbing gas (Lane et al. 2000). Unfortunately due to limited frequency coverage and sensitivity of the receivers available with VLBI such studies cannot be extended to high redshift DLAs. Alternatively, the core fraction measured in the milliarcsecond scale images can be used to get an estimate of the covering factor (see Briggs et al. 1989; Kanekar et al. 2009). Here one assumes that the absorbing gas completely covers at least the emission from the milliarcsec scale core. Therefore, to address this issue, one needs, not only to increase the number of systems searched for 21-cm absorption but also to perform milliarcsecond scale imaging of the background radio sources.

We report here the results of a search for 21-cm absorption in 10 DLAs at $z > 2$ we have carried out using GBT and GMRT, complemented by L-band VLBA images of the background QSOs. This survey has resulted in the detection of 21-cm absorption in the $z_{\rm abs}$= 3.1745 DLA towards J1337+3152. A detailed analysis of this system and two sub-DLAs close to this system are presented in Srianand et al. (2010). Section 2 presents the details of our sample. In Section 3 we present the details of GBT and GMRT spectroscopic observations, VLBA continuum observations, and

Table 1. Log of GBT and GMRT observations to search for 21-cm absorption

Source name	Telescope	Date	Time	BW	Ch.
		yy-mm-dd	(hr)	(MHz)	
(1)	(2)	(3)	(4)	(5)	(6)
J0407−4410	GBT	2006-10-20	4.7	0.625	512
(CTS247)		2007-01-05			
		2007-01-06			
		2007-01-08			
J0733+2721	GBT	2007-12-05	10.7	1.25	512
		2007-12-06			
J0801+4725	GMRT	2006-12-22	10.8	1	128
		2006-11-23			
J0852+2431	GBT	2009-08-07	5.6	1.25	1024
		2009-08-08			
		2009-09-06			
J1017+6116	GBT	2008-10-15	4.5	1.25	1024
		2008-10-16			
		2008-10-18			
J1242+3720	GMRT	2007-06-08	6.1	0.5	128
		2007-06-10			
J1337+3152	GMRT	2009-01-13	6.2	1	128
		2009-03-17	7.8	0.25	128
J1406+3433	GBT	2009-03-05	8.0	1.25	1024
		2009-03-06			
		2009-03-07			
		2009-03-08			
		2009-04-07			
J1435+5435	GMRT	2007-06-10	6.7	1	128

Column 1: Source name. Column 2: Telescope used for 21-cm absorption search. Column 3: Date of observations. Column 4: Total time on source i.e. after excluding telescope set-up time and calibration overheads. Columns 5 and 6: Spectral setup for the observations i.e. bandwidth (BW) and number of spectral channels respectively.

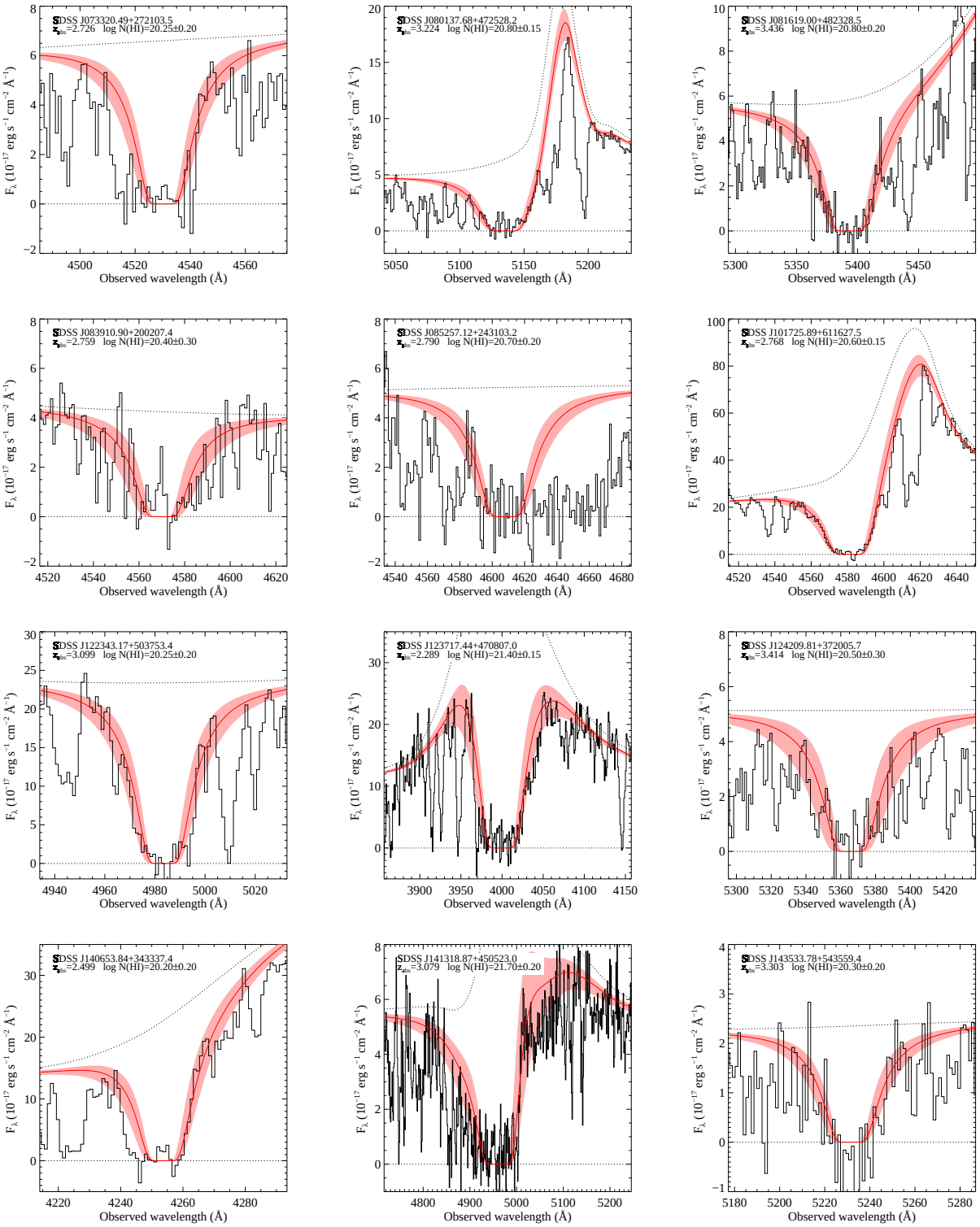

Figure 1. SDSS spectra showing the Lyα lines for 12 DLAs in our sample. The best fitted Voigt profiles (solid curves) together with the associated 1σ errors (shaded regions) are over-plotted. The dotted curve gives the best fitted continuum (in some cases the continuum fit includes the emission lines also). We have used VLT UVES spectra to get N(H I) in the case of $z_{\rm abs}$= 3.1745 system towards J1337+3152 (see Srianand et al. 2010) and $z_{\rm abs}$= 2.595 and 2.622 systems towards J0407−4410 (CTS 247, see Ledoux et al. 2003).

data reduction. The detection rate of 21-cm absorption in DLAs is discussed in Section 4. In Section 5 we study the correlations between the parameters derived from 21-cm observations, N(H I), metallicity and redshift. In Section 6 we study the relation between 21-cm and H_2 absorption. The results are summarized in Section 7. In this work we assume a flat Universe with $H_0 = 71$ km s^{-1} Mpc^{-1}, $\Omega_{\rm m} = 0.27$ and $\Omega_\Lambda = 0.73$.

2 THE SAMPLE OF DLAS

To construct our sample, we cross-correlated the overall sample of DLA-bearing QSO sightlines from SDSS-DR7 (Noterdaeme et al. 2009, including systems that are not part of the published statistical sample used to measure $\Omega_{\rm HI}$) with the VLA FIRST catalog to identify DLAs in front of radio sources brighter than 50 mJy at 1.4 GHz. We excluded radio sources with the DLA 21-cm absorption frequencies redshifted into GBT and GMRT frequency ranges known to be affected by strong radio frequency interference (RFI). There are 13 DLAs from the SDSS-DLA catalog that satisfy these conditions. In addition, there are 4 DLAs along the sight line towards J0407−4410 (also known as CTS 247) at $z_{\rm abs}$ = 1.913, 2.550, 2.595 & 2.622. Two of these, at $z_{\rm abs}$ = 2.595 and 2.622, have redshifted 21-cm absorption frequency in the relatively RFI free frequency range of GBT. Including these two DLAs towards CTS 247, we have a sample of 15 DLAs for which a search for 21-cm absorption was carried-out using either GMRT or GBT. We observed 14 DLAs, (the exception is the $z_{\rm abs}$= 3.079 system towards J1413+4505), but obtained useful spectra for only 10 DLAs. In addition, we have obtained milliarcsecond scale images at 1.4 GHz for all the QSOs except CTS 247 to understand the role of radio structure in detectability of 21-cm absorption in DLAs. The details of the GBT, GMRT and VLBA observations are given below.

The Lyman-α profiles for 12 DLAs selected from the SDSS-DLA catalog are shown in the Fig. 1. The H I column density for each of these DLAs has been estimated using Voigt profile fits to the Lyman-α absorption line. The QSO continuum was approximated by a lower order spline using absorption free regions on both sides of the H I trough (dotted curves in each panel). In addition, special care was taken to fit the emission line profiles whenever the Lyα absorption is close to QSO emission lines. For the remaining three DLAs in our sample, $z_{\rm abs}$=3.1745 DLA towards J1337+3152 and the two DLAs towards CTS 247, we use the column densities measured by Srianand et al. (2010) and Ledoux et al. (2003) respectively from high resolution VLT UVES spectra.

3 DETAILS OF OBSERVATIONS AND DATA REDUCTION

3.1 The GBT and GMRT observations

We observed our sample of 14 DLAs using the GBT prime focus receivers PF1-340 MHz and PF1-450 MHz, and the GMRT P-band receiver. Although we selected DLAs such that the redshifted 21-cm absorption frequencies were not affected by strong RFI, no useful data could be obtained for 4 absorption systems either due to RFI or other technical reasons. The observing log for the remaining 10 DLAs and the spectral set-up used for these observations are provided in Table 1. GBT observations were performed in the standard position-switching mode with typically 5 min spent on-source and 5 min spent off-source. The data were acquired in the orthogonal polarization channels XX and YY. We used the GBT spectral processor as the backend for these observations. The two DLAs towards CTS 247 were observed simultaneously using two bands of 0.625 MHz split into 512 channels. For the GMRT observations, typically a bandwidth of 0.5 or 1 MHz split into 128 frequency channels was used. The data were acquired in the two orthogonal polarization channels RR and LL. For the flux density/bandpass calibration of GMRT data, standard flux density calibrators were observed for 10-15 min every two hours. A phase calibrator was also observed for 10 min every ∼45 min to get reliable phase solutions.

We used NRAO's GBTIDL package to develop a pipeline to automatically analyse the GBT spectral-line data sets. After excluding time ranges for which no useful data were obtained, the data were processed through this pipeline. The pipeline calibrates each data record individually and flags the spectral channels with deviations larger than 5σ as affected by RFI. After subtracting a second order baseline these data are averaged to produce baseline (i.e. continuum) subtracted spectra for XX and YY. The baseline fit and statistics for the flagging are determined using the spectral region that excludes the central 25% and last 10% channels at both ends of the spectrum. If necessary, a first-order cubic spline was fitted to the averaged XX and YY spectra obtained from the pipeline, which were then combined to produce the Stokes-I spectrum. The spectrum was then shifted to the heliocentric frame. The multi-epoch spectra for a source were then resampled onto the same frequency scale and combined to produce the final spectrum.

The GMRT data were reduced using the NRAO AIPS package following the standard procedures described in Gupta et al. (2006). Special care was taken to exclude the baselines and time stamps affected by RFI. The spectra at the quasar positions were extracted from the RR and LL spectral cubes and compared for consistency. If necessary, a first-order cubic-spline was fitted to remove the residual continuum from the spectra. The two polarization channels were then combined to get the stokes I spectrum which was then shifted to the heliocentric frame.

The FWHM of the GBT beam at 400 MHz is 30′ and the rms confusion is 500 mJy. This is comparable to the flux densities of the background radio sources observed with the GBT. Therefore, to correct for the effect of other confusing sources in the GBT beam and determine the QSO flux densities at the redshifted 21-cm frequency, we observed these with the GMRT at 610 and 325 MHz. For these observations we have used 32 MHz bandwidth. Details of these GMRT observations and the measured flux densities are provided in Table 2. For J1406+3433, the 325 MHz flux density is taken from the Westerbork Northern Sky Survey (WENSS). We interpolate these flux density measurements to determine the flux densities at redshifted 21-cm frequencies for the quasars observed with the GBT. Since, flux densities for these 5 QSOs are not measured at the same epoch as the GBT spectroscopic observations, in principle, radio flux density variability can affect our estimates of 21-cm optical

Table 2. GMRT low-frequency flux density measurements for the DLAs observed with the GBT

Source name	$S_{610\rm MHz}$	Date	$S_{325\rm MHz}$	Date
	(mJy)	yy-mm-dd	(mJy)	yy-mm-dd
(1)	(2)	(3)	(4)	(5)
J0407−4410	124	2006-05-23	52	2007-11-24
J0733+2721	248	2007-11-04	549	”
J0852+2431	198	2008-12-26	237	2009-03-17
J1017+6116	274	”	266	,,
J1406+3433	165	”	185†	(WENSS)

Column 1: Source name. Columns 2 and 4: GMRT flux density measurements at 610 and 325 MHz respectively. Columns 3 and 5: Dates of the 610 and 325 MHz observations respectively.
† From the WENSS catalog.

Table 3. Results from the GBT and GMRT observations

Source name	$z_{\rm em}$	$z_{\rm abs}$	$\log N$(H I)	$S_{1.4\,GHz}$	δ	Spectral rms	$S_{\nu_{abs}}$	$\int \tau {\rm dv}$	$\frac{T_{\rm s}}{f_{\rm c}}$
			($\rm cm^{-2}$)	(mJy)	($\rm km\,s^{-1}$)	($\rm mJy\,b^{-1}\,ch^{-1}$)	(mJy)	($\rm km\,s^{-1}$)	(K)
(1)	(2)	(3)	(4)	(5)	(6)	(7)	(8)	(9)	(10)
J040718−441013	3.020	2.595	21.05±0.10	-	3.7	5.9	67	<1.61	>382
J040718−441013	”	2.622	20.45±0.10	-	”	7.1	67	<1.93	>81
J073320.49+272103.5	2.938	2.7263	20.25±0.20	240	3.8	3.4	451	<0.14	>692
J080137.68+472528.2	3.276	3.2235	20.80±0.15	78	7.0	1.5	164	<0.22	>1563
J085257.12+243103.2	3.617	2.7902	20.70±0.20	160	3.9	3.9	228	<0.32	>850
J101725.89+611627.5	2.805	2.7681	20.60±0.15	477	3.9	4.2	268	<0.29	>758
J124209.81+372005.7	3.839	3.4135	20.50±0.30	662	3.6	3.6	615	<0.11	>1567
J133724.69+315254.5	3.174	3.1745	21.36±0.10	83	6.9	1.3	69	2.08±0.17	600^{+220}_{-160}
J140653.84+343337.4	2.566	2.4989	20.20±0.20	167	3.6	3.0	178	<0.31	>356
J143533.78+543559.4	3.811	3.3032	20.30±0.20	96	7.1	1.5	145	<0.26	>418

Column 1: Source name. Column 2: QSO emission redshift. Column 3: Absorption redshift of DLAs as determined from the metal absorption lines. Column 4: H I column density. Column 5: Flux density at 1.4 GHz from the FIRST catalog. Columns 6 and 7: Spectral resolution and rms for the survey spectrum. Column 8: Continuum flux density of source at the redshifted 21-cm absorption frequency. Column 9: Integrated 21-cm optical depth or 3-sigma upper limit to $\int \tau dv$ for the equivalent spectral resolution of $10\,\rm km\,s^{-1}$. Column 10: Ratio of spin temperature and covering factor of absorbing gas.

depths for the corresponding DLAs. However, this effect is much smaller than the error caused by confusion from other sources in the beam and should not affect the statistical results derived later in the paper.

The GBT and GMRT observations of our DLA sample have resulted in useful 21-cm absorption spectra for 10 DLAs. These spectra are presented in Fig. 2. GBT spectra, typically acquired at a spectral resolution, of $\sim$1 km s^{-1}have been smoothed to $\sim$4 km s^{-1}for presentation. The 21-cm absorption is detected only for one DLA (i.e. $z_{\rm abs} = 3.1745$ DLA towards J1337+3152) and a detailed analysis of this system is presented in Srianand et al. (2010). None of the other “absorption-like features”, marked as shaded regions, are reproduced in spectra from different polarizations and epochs, but are due to RFI. For CTS247b (i.e for $z_{\rm abs}$= 2.622 DLA towards CTS247) these features are present only in one polarization at certain times. For J0852+2431 and J1017+6116, using a combination of high spectral resolution ($\sim$1 km s^{-1}) and/or multi-epoch observations we rule out the possibility of these features being real 21-cm absorption. Details of the optical depth measurements and other observational results for all the 10 DLAs are summarized in Table 3.

3.2 Continuum observations with VLBA

The sample of quasars presented here was observed as part of a larger VLBA survey to obtain milliarcsecond scale images for QSOs with foreground DLAs and Mg II systems, and understand the relationship between radio structure and detectability of 21-cm absorption. We have observed using VLBA 21-cm receiver for 11 hrs and 18 hrs on 21/02/2010 and 10/06/2010 respectively. We used eight 8 MHz baseband channels, i.e. the total bandwidth of 64 MHz. Each baseband channel was split into 32 spectral points. Both the right and left-hand circular polarization channels were recorded. Two bit sampling and a post-correlation time resolution of 2 seconds were used.

The observations were done using nodding-style phase-referencing with a cycle time of $\sim$5 min, i.e. 3 min on the source and $\sim$1.5 min on the phase-referencing calibrator. The phase-referencing calibrators were selected from the VLBA calibrator survey (VCS) at 2.3 and 8.6 GHz (Table 4). In order to improve the uv-coverage, the total observing time was split into snapshots over a number of different hour angles. Each source, except CTS247 which was excluded due to observational constraints, was typically observed for a total of $\sim$30 min. During both observing runs, strong fringe find-

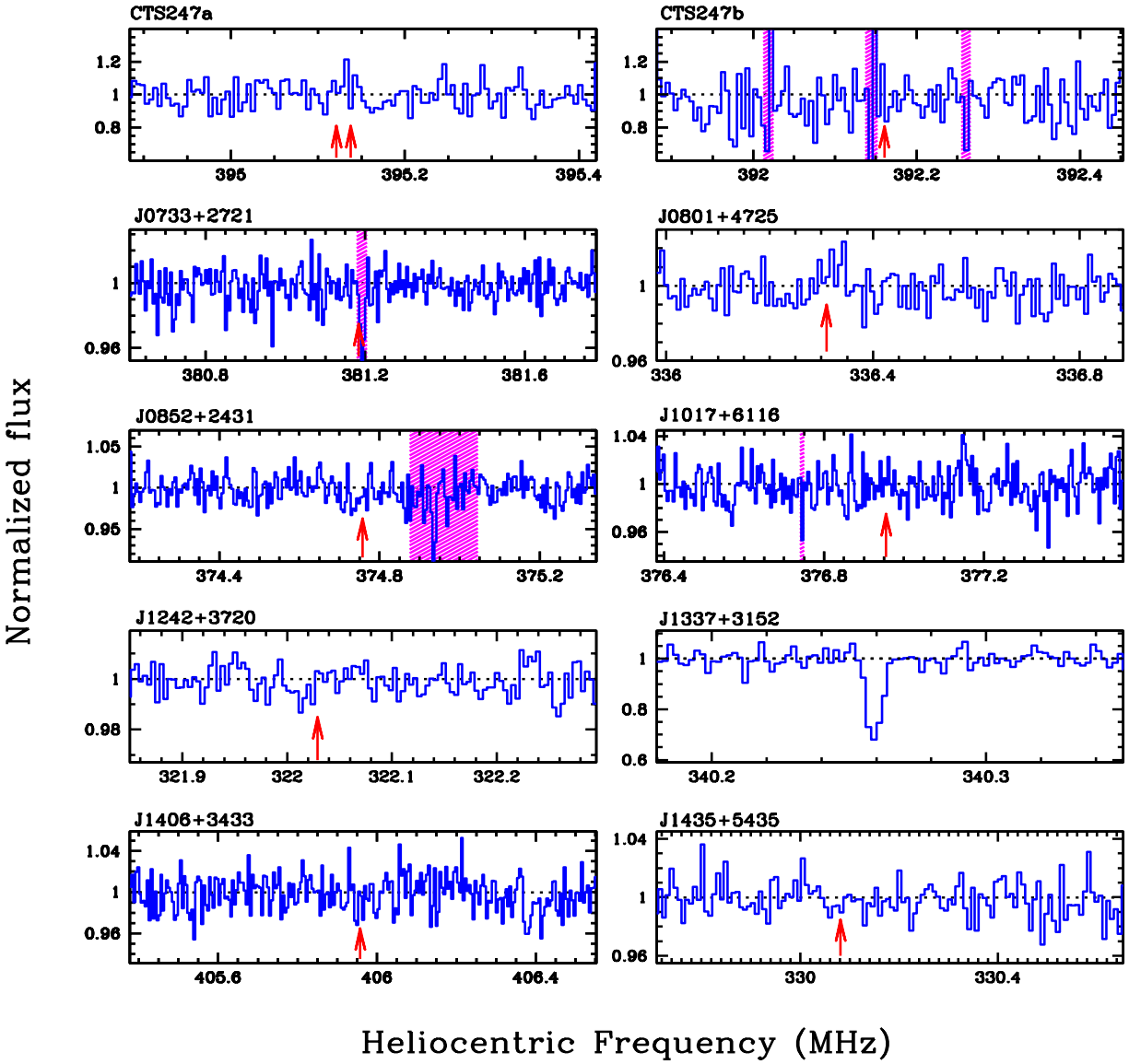

Figure 2. GBT and GMRT spectra of DLAs in our sample. Shaded regions mark features that are due to RFI. The arrows in the case of non-detections indicate the expected positions of the 21-cm absorption. In the case of $z_{\rm abs}$= 3.1745 system towards J1337+3152 we show the high resolution 21-cm absorption spectrum only. Two arrows in the case of CTS247a indicate the expected position of 21-cm absorption from the two H_2 components.

ers/bandpass calibrators such as J0555+3948, J0927+3902, J1800+3848 and J2253+1608 were also observed every ∼3 hr for 4-5 min.

Data were calibrated and imaged using AIPS and DIFMAP in a standard way. Global fringe fitting was performed on the phase-referencing calibrators. The delays, rates and phases estimated from these were transferred to the sources which were then self-calibrated until the final images were obtained. Radio sources were characterised by fitting Gaussian models to the self-calibrated visibilities. VLBA maps of the 13 QSOs are shown in Fig. 3 and the results of model fitting are listed in columns # 6-12 of Table 3.2.

Non-detection of 21-cm absorption in a DLA could be due to the small covering factor of the absorbing gas. The typical spatial resolution achieved in our VLBA observations is ∼8 mas. If the extent of absorbing gas is of the order of the scales probed by our VLBA observations (i.e. >20pc) then we expect the detectability of 21-cm absorption to depend on the fraction and spatial extent of radio flux density detected in these images. In column # 14 of Table 3.2 we give the ratio of total flux densities detected in the VLBA and FIRST images at 20cm, i.e. $f_{\rm VLBA}$. The last column of this table gives the largest linear size (LLS), i.e the separation between the farthest radio components, of the radio source at the redshift of the DLA. Out of the 13 QSOs presented in Fig. 3 that have DLAs along their line of sight, we have 21-cm absorption spectra for only 8 DLAs. For the DLA to-

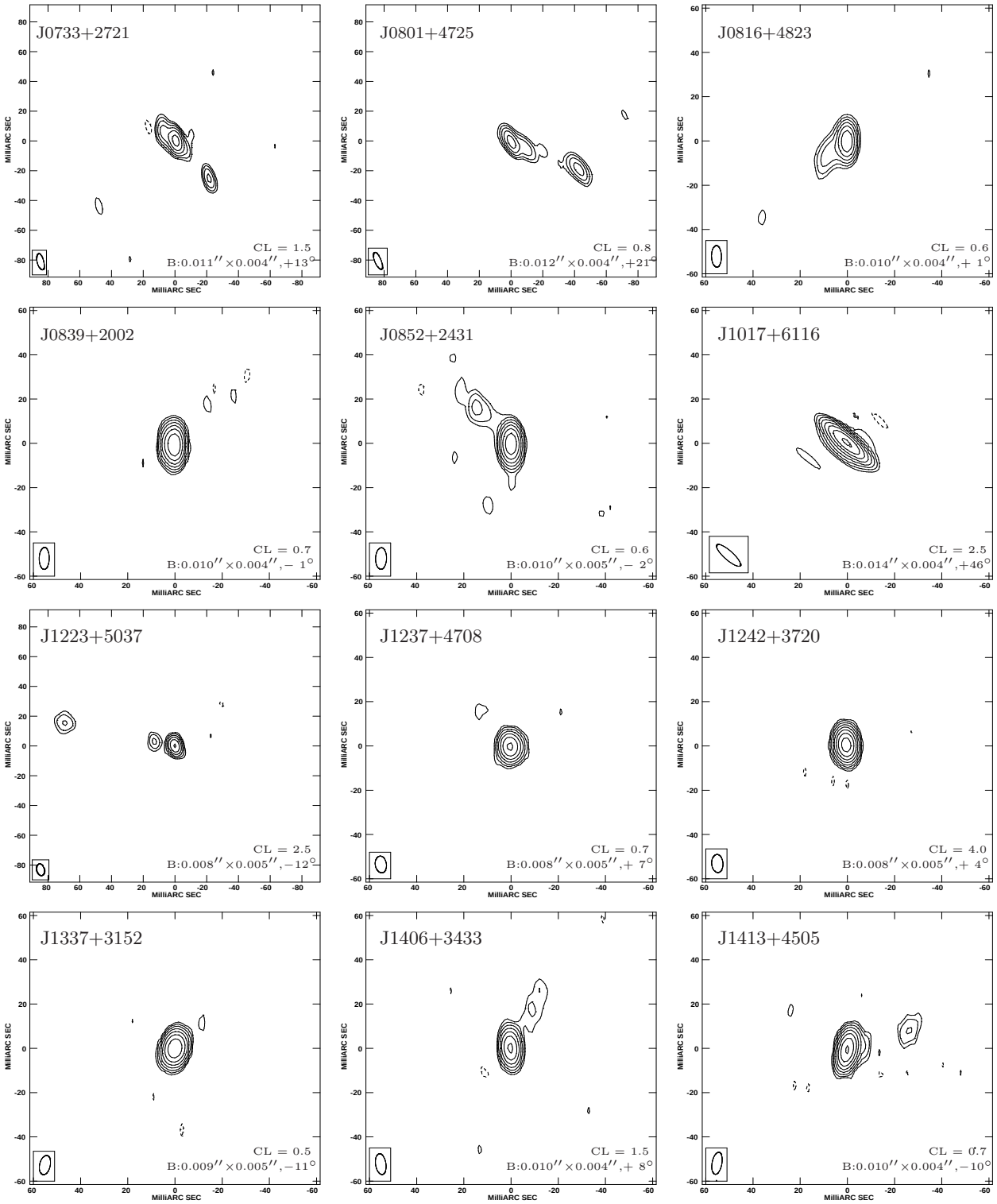

Figure 3. Contour plots of VLBA images at 1.4 GHz. The rms in the images are listed in Table 3.2. At the bottom of each image the restoring beam is shown as an ellipse, and the first contour level (CL) in mJy beam^{-1} and FWHM are noted. The contour levels are plotted as CL×(−1, 1, 2, 4, 8,...) mJy beam^{-1}. Depending upon the detailed structure of the radio sources, the emission could be more extended at the redshifted 21-cm frequencies.

Table 5: Results from the VLBA data.

Source name	$z_{\rm abs}$	Right ascension (J2000)	Declination (J2000)	rms (mJy beam^{-1})	Comp.	S (mJy)	r (mas)	θ (°)	a (mas)	b/a	ϕ (°)	$S_{\rm T}$ (mJy)	$f_{\rm VLBA}$	LLS (pc)
(1)	(2)	(3)	(4)	(5)	(6)	(7)	(8)	(9)	(10)	(11)	(12)	(13)	(14)	(15)
J0733+2721	2.7263	07 33 20.4830	+27 21 03.430	0.3	1	97	0	-	4.52	0.05	-88	240	0.62	348
					2	3	9.1	-129	13.24	0.00	-18			
					3	19	32.7	-140	5.98	0.26	32			
					4	29	10.8	51	8.37	0.44	-17			
J0801+4725	3.2235	08 01 37.6930	+47 25 28.082	0.2	1	28	0	-	6.77	0.00	72	78	0.67	342
					2	8	9.34	-112	7.09	0.00	72			
					3	16	44.7	-112	8.63	0.22	64			
J0816+4823		08 16 19.0044	+48 23 28.490	0.2	1	42	0	-	4.59	0.24	87	69	0.75	68
					2	10	9.0	132	8.75	0.43	-63			
J0839+2002		08 39 10.8970	+20 02 07.391	0.2	1	113	0	-	4.91	0.24	84	130	0.87	$\leq$39
J0852+2431	2.7902	08 52 57.1211	+24 31 03.271	0.2	1	78	0	-	4.92	0.31	71	160	0.55	175
					2	10	21.9	42	15.2	0.16	53			
J1017+6116	2.7681	10 17 25.8865	+61 16 27.414	0.5	1	388	0	-	1.50	0.68	55	477	0.86	38
					2	24	4.7	145	2.45	0.00	70			
J1223+5037		12 23 43.1740	+50 37 53.344	0.5	1	96	0	-	2.50	0.00	78	229	0.60	554
					2	16	13.6	80	3.01	0.83	-19			
					3	25	71.4	78	8.61	0.00	89			
J1237+4708		12 37 17.4413	+47 08 06.964	0.2	1	64	0	-	3.17	0.20	-74	80	0.80	$\leq$ 27
J1242+3720	3.4135	12 42 09.8121	+37 20 05.692	0.6	1	848	0	-	1.93	0.76	22	662	1.00	$\leq$ 14
J1337+3152	3.1747	13 37 24.6931	+31 52 54.642	0.2	1	83	0	-	3.85	0.38	74	83	1.00	$\leq$ 30
J1406+3433	2.4989	14 06 53.8532	+34 33 37.339	0.4	1	127	0	-	3.24	0.22	-23	167	0.87	153
					2	18	18.7	-30	23.79	0.23	-25			
J1413+4505		14 13 18.8652	+45 05 22.990	0.2	1	105	0	-	2.19	0.42	-67	140	0.88	216
					2	12	3.4	-77	5.37	0.00	-86			
					3	6	27.9	-72	6.28	0.03	-67			
J1435+5435	3.3032	14 35 33.7812	+54 35 59.312	0.2	1	31	0	-	2.66	0.17	-29	96	0.55	155
					2	17	20.4	155	4.00	0.47	-36			
					3	5	7.6	153	5.52	0.00	-7			

Column 1: Source name. Column 2: absorption redshift. Columns 3 and 4: right ascension and declination of component-1 (see column 6) from the multiple Gaussian fit to the source, respectively. Column 5: rms in the map in mJy beam^{-1}. Column 6: component id. Column 7: flux density of the component in mJy. Columns 8 and 9: radius and position angle of the component with respect to component-1, respectively. Columns 10, 11 and 12: major axis, axial ratio and position angle of the deconvolved Gaussian component, respectively. Column 13: flux density in mJy from FIRST/NVSS. Column 14: c_f is the ratio of 1.4 GHz flux density in VLBA image to that in the FIRST image, Column 15: largest projected linear size in pc.

Table 4. Details of phase-referencing calibrators used for the VLBA observations

Source	Calibrator	Separation (degrees)
(1)	(2)	(3)
J0733+2721	J0732+2548	1.5
J0801+4725	J0754+4823	1.5
J0816+4823	J0808+4950	1.9
J0839+2002	J0842+1835	1.6
J0852+2431	J0856+2111	3.5
J1017+6116	J1031+6020	2.0
J1223+5037	J1227+4932	1.3
J1237+4708	J1234+4753	0.9
J1242+3720	J1242+3751	0.5
J1337+3152	J1329+3154	1.6
J1406+3433	J1416+3444	1.9
J1413+4505	J1417+4607	1.2
J1435+5435	J1429+5406	1.0

Column 1: Source name. Column 2: Phase-referencing calibrator. Column 3: Separation between the radio source and phase-referencing calibrator.

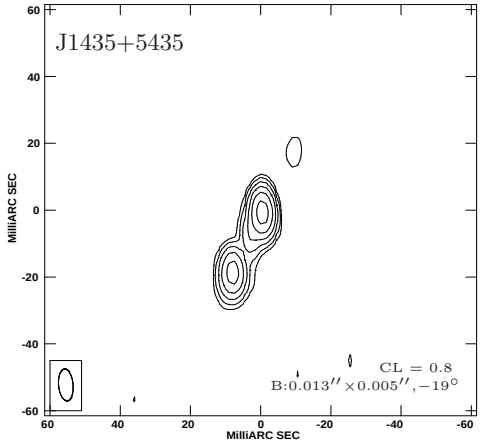

Figure 3. *Continued.*

wards J0816+4823, we use the 21-cm absorption measurement from Curran et al. (2010). Thus we have a sample of 9 DLAs with both 21-cm absorption measurements and VLBA 21-cm maps for the background QSOs. The $f_{\rm VLBA}$ for this sample ranges from 0.6 to 1, and LLS from <15 pc to 340 pc.

In the absence of VLBI spectroscopy at the redshifted 21-cm line frequency, the ratio of VLBA core flux density to the total flux density measured in the arcsecond scale images (called core fraction c_f) has been used as an indicator of the covering factor f_c (see Briggs et al. 1989; Kanekar et al. 2009). Here we use the term 'core' to refer to the flat spectrum unresolved radio component coincident with the optical QSO in the VLBA image.

For J1242+3720 and J1337+3152 the radio source is modelled as a single unresolved component and within the uncertainties all the flux density in the arcsecond scale FIRST images is recovered in our VLBA images (Fig. 3). Both of these sources, have flat spectra suggesting the radio emission even at lower frequencies originates predominantly from the compact core. Therefore we take f_c=1 for this case.

The radio source J1017+6116 has an inverted radio

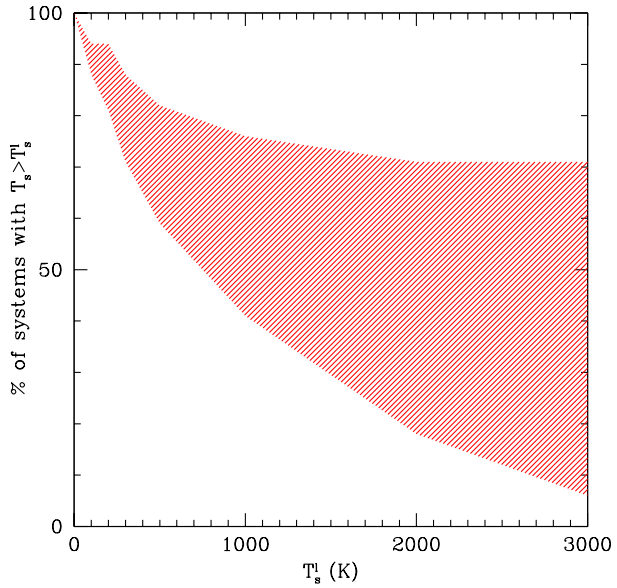

Figure 4. The allowed range of fraction of DLAs having harmonic mean spin temperature $T_{\rm S}$ greater than a limiting value $T_{\rm S}^l$ as a function of $T_{\rm S}^l$. We use only those DLAs for which c_f measurements are available. The lower envelope of the shaded region is obtained considering all the lower limits on $T_{\rm S}$ as measurements. The upper envelope is obtained assuming all the lower limits as measurements with $T_{\rm S} \geq T_{\rm S}^l$.

spectrum (α=−0.4) and 86% of the flux density in the FIRST image is recovered in the VLBA image, 94% of which is contained in the main unresolved component (Fig. 3). For another 3 flat-spectrum sources with 21-cm absorption measurements, i.e. J0816+4823, J0852+2431, and J1406+3433, more than 80% of the VLBA flux density is present in a single unresolved component. For these 4 sources, based on the flat spectral index, the dominant component in the VLBA image can be identified with radio core/optical QSO. Therefore for the 6 sources mentioned above, we have estimated the core fraction, c_f, and used it as the covering factor, f_c, of the gas. The remaining three sources, J0733+2721, J0801+4725 and J1435+5435, exhibit multiple components in their VLBA 20-cm images. The identification of the component coincident with the QSO, and the estimation of their c_f from VLBA images for these three sources are highly uncertain.

4 DETECTABILITY OF 21-CM ABSORPTION

In this Section we investigate the detectability of 21-cm absorption in DLAs and the implication of non-detections for the physical state of the H I gas. It is clear from the last column of Table 3, that for most of the DLAs, our data has good sensitivity to detect $T_{\rm S}/f_c$∼100 K gas.

The H I 21-cm absorption is detected only in the $z_{\rm abs}$ = 3.1745 system towards SDSS J1337+3152. This is one of the weakest radio sources in our sample (with a 3σ $\int \tau dv$ limit of 0.4 km s^{-1}). However, thanks to high N(H I) our spectrum is sensitive enough to detect any gas with $T_{\rm S} \leq$ 3100 K. This source is unresolved in our VLBA observations (see Fig 3). The L-band flux density measured in

our VLBA image is consistent with that measured by the FIRST survey. Therefore, the core fraction is, $c_{\rm f} \sim 1$, and the size of the VLBA beam is less than 30 pc at the redshift of the absorber. The spin-temperature, measured from the ratio of 21-cm optical depth and the N(H I) column density derived from the Lyman-α trough, is 600^{+220}_{-160} K which is consistent with the upper limit on $T_{\rm S}$ obtained from the width of the single component Gaussian fit to the 21-cm absorption (Srianand et al. 2010).

In Table 6 we provide various details of our measurements together with the previous measurements at $z \geq 2$ from the literature. We present the results dividing the sample into three groups. These are systems with 21-cm detections (five systems), systems with 21-cm absorption upper limits with (twelve systems) and without (eleven systems) high-resolution optical spectra from which to derive accurate metallicities. The first two groups are used to investigate the connection between UV measurements and 21-cm optical depth. In all cases the 3σ upper limits on the integrated 21-cm optical depth are computed assuming a line width of 10 km s^{-1}.

The 21-cm detection rate from our sample, without putting any sensitivity limit, is 10%. This is 13% when we restrict to $\int \tau dv$ limit of 0.4 km s^{-1}(the limit achieved in the case of J1337+3152 where we have 21-cm detection). Taken at face value, the extended sample listed in Table 6 gives a 21% detection rate for $\int \tau dv$ limit of 0.4 km s^{-1}. For a $\int \tau dv$ limit of 0.2 km s^{-1}we get the detection rate of 28%. However, these may not be representative values as the list of systems compiled from the literature may be biased towards detections as some authors may not have reported their non-detections systematically

Since we know N(H I) from the damped Lyman-α line, the detection limit on the integrated optical depth implies a lower limit on the ratio $T_{\rm S}/f_{\rm c}$. The $T_{\rm S}/f_{\rm c}$ measurements are reported in column 7 of Table 6. In column 6 of this table, we give the core fraction c_f. As mentioned above, c_f is basically the ratio of flux density in the unresolved core seen in VLBA images to the total flux density measured in the arcsecond scale FIRST images. For the objects from the literature we use the c_f values given in Kanekar et al. (2009). These measurements were made at 327 MHz, close to the redshifted 21-cm frequencies. Following Kanekar et al. (2009) we use core fraction (c_f) as the estimate of the covering factor (f_c). The $T_{\rm S}$ measurements given in column 8 of Table 6 are obtained by assuming $f_c = c_f$.

In Fig. 4 we plot the percentage of DLAs having $T_{\rm S}$ greater than a limiting value $T_{\rm S}^l$ as a function of $T_{\rm S}^l$ for systems with $T_{\rm S}$ measurements given in column 8 of Table 6. The lower envelope of the shaded region is obtained considering all the lower limits on $T_{\rm S}$ as measurements. The upper envelope is obtained assuming all the lower limits as measurements with $T_{\rm S} \geq T_{\rm S}^l$. It is clear from the figure that more than 50% of the DLAs have $T_{\rm S} \geq 700K$. Remember that the $T_{\rm S}$ measured in an individual DLA is the harmonic mean temperature of different phases that contribute to the observed N(H I). Assuming that the gas is simply a two phase medium with similar covering factors the fraction of H I in the CNM (called f(CNM)) can be written as,

$$f({\rm CNM}) = \frac{1}{T_{\rm S}^W}\left[\frac{T_{\rm S}^{\rm C}T_{\rm S}^W}{T_{\rm S}} - T_{\rm S}^{\rm C}\right] \quad (1)$$

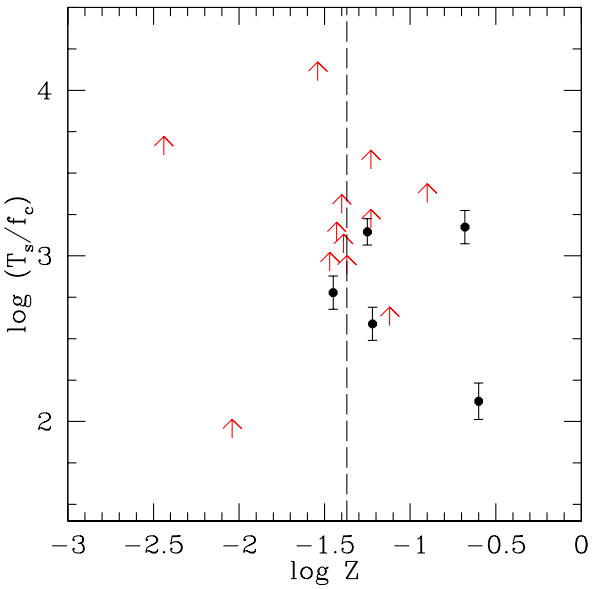

Figure 5. Metallicity vs T_S/f_c. The vertical dashed line marks the median metallicity measured in our sample.

where, $T_{\rm S}^{\rm C}$ and $T_{\rm S}^{\rm W}$ are the spin-temperature of the CNM and WNM respectively. Srianand et al. (2005) have noticed that the H I phase traced by the H_2 absorption has temperature typically in the range 100-200 K. Thus we consider the CNM temperature to be 200 K (instead of 70 K as seen in CNM of the Galaxy) so that the f(CNM) we get will be a conservative upper limit. Assuming $T_{\rm S}^{\rm C} \sim 200$ K and $T_{\rm S}^{\rm W} \sim 10^4$ K, $T_S = 700$ K can be obtained for a combination of f(CNM) = 0.27 and f(WNM) = 0.73. Therefore f(CNM) is less than 0.27 in at least 50% of the DLAs. Note that choosing $T_{\rm S}^{\rm W} \sim 8000$ K (as suggested for the Galactic ISM) instead of the 10^4 K used here, does not change the results appreciably.

We estimate f(CNM) for the four 21-cm detections (excluding J0501-0159 (B0458-020) for which we do not have the covering factor value). Apart from J0314+4314 (3C082) which seems to be a special case (York et al. 2007), the CNM seems to represent roughly 20 to 30% of the total N(H I) measured in these DLAs. For individual non-detections, we can calculate conservative upper limits of the fraction of N(H I) in the CNM phase assuming $T_{\rm S}^{\rm C} = 200$ K. The values of f(CNM) are given in column #9 of Table 6 for systems with $f_{\rm c}$ measurements. The upper limits vary between 0.10 and 1.0 with a median value of 0.23. Thus the analysis presented here, under the assumption that $f_c = c_f$, suggests that most of the neutral hydrogen in high-z DLAs is warm. This is very much consistent with the conclusion of Petitjean et al. (2000) based on the lack of H_2 detections in most high-z DLAs.

5 RESULTS OF CORRELATION ANALYSIS

In this Section we explore correlations between the 21-cm optical depth and other observable parameters. As we have only a few 21-cm detections and mostly upper limits we use survival analysis and in particular the generalised rank

Table 6. Summary of 21-cm searches in $z \geq 2$ DLAs. Column 1: QSO. Column 2: absorption redshitft. Column 3: log N(H I). Column 4: Integrated optical depth. Column 5: Reference for $\int \tau dv$ given in column 4. Column 6: the core fraction c_f. Column 9: the fraction of CNM (see the text for its definition). Column 10: the H_2 fraction and Column 11: References for N(H I) and/or f(H_2) measurements.

QSO	$z_{\rm abs}$	log$N$(H I)	$\int \tau dv$ (km s^{-1})	Refs	c_f	$T_{\rm S}/f_{\rm c}$ (K)	$T_{\rm S}$ (K)	f(CNM)	log f(H_2)	Refs
(1)	(2)	(3)	(4)	(5)	(6)	(7)	(8)	(9)	(10)	(11)
21-cm detections										
J020346.6+113445	3.38714	21.26± 0.08	0.71±0.02	1	0.76	1397	1062	∼0.19	$-6.2, -4.6$	a
J031443.6+431405	2.28977	20.30± 0.11	0.82±0.09	2	....	133	....	∼1.00	....	d
J044017.2−433309	2.34747	20.78± 0.10	0.22±0.03	3	0.59	1493	881	∼0.23	....	e
J050112.8−015914	2.03955	21.70± 0.10	7.02±0.16	4	....	390	...	....	≤ -6.40	b
J133724.6+315254	3.17447	21.36± 0.10	2.08±0.17	5	1.00	600	600	∼0.33	-7.00	c
21-cm non-detections having metallicity measurements										
J033755.7−120412	3.1799	20.65± 0.10	≤0.06	6	0.62	≥4057	≥2515	≤ 0.08	≤ −5.10	b
J033901.0−013318	3.0619	21.10± 0.10	≤0.06	6	0.68	≥11435	≥7775	≤ 0.03	≤ −6.90	b
J040733.9−330346	2.569	20.60± 0.10	≤0.12	7	0.44	≥1807	≥795	≤ 0.25	....	e
J040718.0−441013	2.59475	21.05± 0.10	≤1.61	8	....	≥380	....	....	$-2.61^{+0.17}_{-0.20}$	b
J040718.0−441013	2.62140	20.45± 0.10	≤1.93	8	....	≥80	....	....	≤ −6.20	b
J043404.3−435550	2.30197	20.95± 0.10	≤0.33	7	....	≥1471	....	....	≤ −5.15	b
J053007.9−250330	2.81115	21.35± 0.07	≤0.58	9†	0.94	≥2103	≥1977	≤ 0.10	$-2.83^{+0.18}_{-0.19}$	b
J091551.7+000713	2.7434	20.74± 0.10	≤0.37	7	....	≥809	....	....	....	e
J135646.8−110129	2.96680	20.80± 0.10	≤0.33	6	....	≥1042	....	....	≤ −6.75	b
J135706.1−174402	2.77990	20.30± 0.15	≤0.14	7	....	≥777	....	....	≤ −5.99	a
J142107.7−064356	3.44828	20.50± 0.10	≤0.14	7	0.69	≥1231	≥849	≤ 0.24	≤ −5.69	b
J234451.2+343348	2.90910	21.11± 0.10	≤0.21	6	0.71	≥3343	≥2373	≤ 0.08	≤ −6.19	a
21-cm non-detections having no metallicity measurements										
J053954.3−283956	2.9742	20.30± 0.11	≤0.06	6	0.47	≥1812	≥ 851	≤ 0.23	....	e
J081618.9+482328	3.4358	20.80± 0.20	≤1.43	9	0.60	≥240	≥ 144	≤ 1.00	....	a
J073320.4+272103	2.7263	20.25± 0.20	≤0.14	8	....	≥692	....	....	....	a
J080137.6+472528	3.2235	20.80± 0.15	≤0.22	8	....	≥1563	....	....	....	a
J085257.1+243103	2.7902	20.70± 0.20	≤0.32	8	0.49	≥854	≥ 418	≤ 0.48	....	a
J101725.8+611627	2.7681	20.60± 0.15	≤0.29	8	0.81	≥748	≥ 606	≤ 0.33	....	a
J124209.8+372005	3.4135	20.50± 0.30	≤0.11	8	1.00	≥1566	≥ 1566	≤ 0.13	....	a
J140501.1+041536	2.708	21.07± 0.24	≤0.19	9	....	≥3369	....	....	....	f
J140501.1+041536	2.485	20.20± 0.20	≤0.08	9	....	≥1080	....	....	....	f
J140653.8+343337	2.4989	20.20± 0.20	≤0.31	8	0.76	≥279	≥ 212	≤ 0.94	....	a
J143533.7+543559	3.3032	20.30± 0.20	≤0.26	8	....	≥418	....	....	....	a

References in column #5: 1) Kanekar et al. (2007), 2) York et al. (2007), 3) Kanekar et al. (2006), 4) Briggs et al. (1989), 5) Srianand et al. (2010), 6) Kanekar & Chengalur (2003), 7) Kanekar et al. (2009), 8) This paper, and 9) Curran et al. (2010). † Archival data from GBT08A_003 (PI: Curran) was processed through our pipeline. See text for details.
References for N(H I) and/or f(H_2) measurements (column # 11): a) This paper, b) Noterdaeme et al. (2008), c) Srianand et al. (2010), d) Ellison et al. (2008), e) Akerman et al. (2005) f) Curran et al. (2010).

correlation test (Isobe et al. 1986). For this purpose we use the Astronomical SURVival analysis (ASURV) package.

5.1 Metallicity vs T_s/f_c

Firstly we study the importance of the metallicity of the gas. Only 3 DLAs in our sample have measurements of metallicity from high resolution optical spectroscopy. In the extended sample at $z \geq 2$ (see Table 6) there are 17 systems with metallicity measurements and 21-cm spectra. In Fig. 5, we plot $T_{\rm S}/f_{\rm c}$ versus metallicity. The vertical long-dashed line marks the median metallicity of the points plotted in the figure. The only detection found in the low metallicity half is for $z_{\rm abs} = 3.1745$ towards J1337+3152 reported from our survey. The other four detections are from the high metallicity half. The non-parametric generalized Kendall rank correlation test suggests only a weak correlation between Z and $T_{\rm S}/f_{\rm c}$ (at the 1.42σ level) with the probability that it can arise due to chance being 0.15. The significance is even lower (i.e 0.9σ with a chance probability of 0.37) when we use $T_{\rm S}$ (instead of $T_{\rm S}/f_{\rm c}$) for cases where we have estimated $f_{\rm c}$ measurements. We wish to point out that a correlation between T_s/f_c and metallicity is reported in the literature (Curran et al. 2007; Kanekar et al. 2009; Curran et al. 2010). The lack of correlation in our sample (with systems in a restricted redshift range) could either reflect redshift evolution of the relationship or small range in metallicity covered by the sample. Metallicity measurements for the remaining 11 systems in Table 6 would allow us to address this issue in a statistically significant manner.

We also looked at the possible correlation between the 21-cm optical depth and the velocity width (Δv) of the low ionization lines. This information is available for 14 sources. Again we find no statistically significant correlation between the two. This is inconsistent with the 2.2 to 2.8 σ level weak correlation between W(Mg II) and Δv reported by Curran et al. (2007). However, this is consistent with the finding of Gupta et al. (2009), that W(Mg II) and 21-cm optical depth are not correlated for a sample of 33 strong

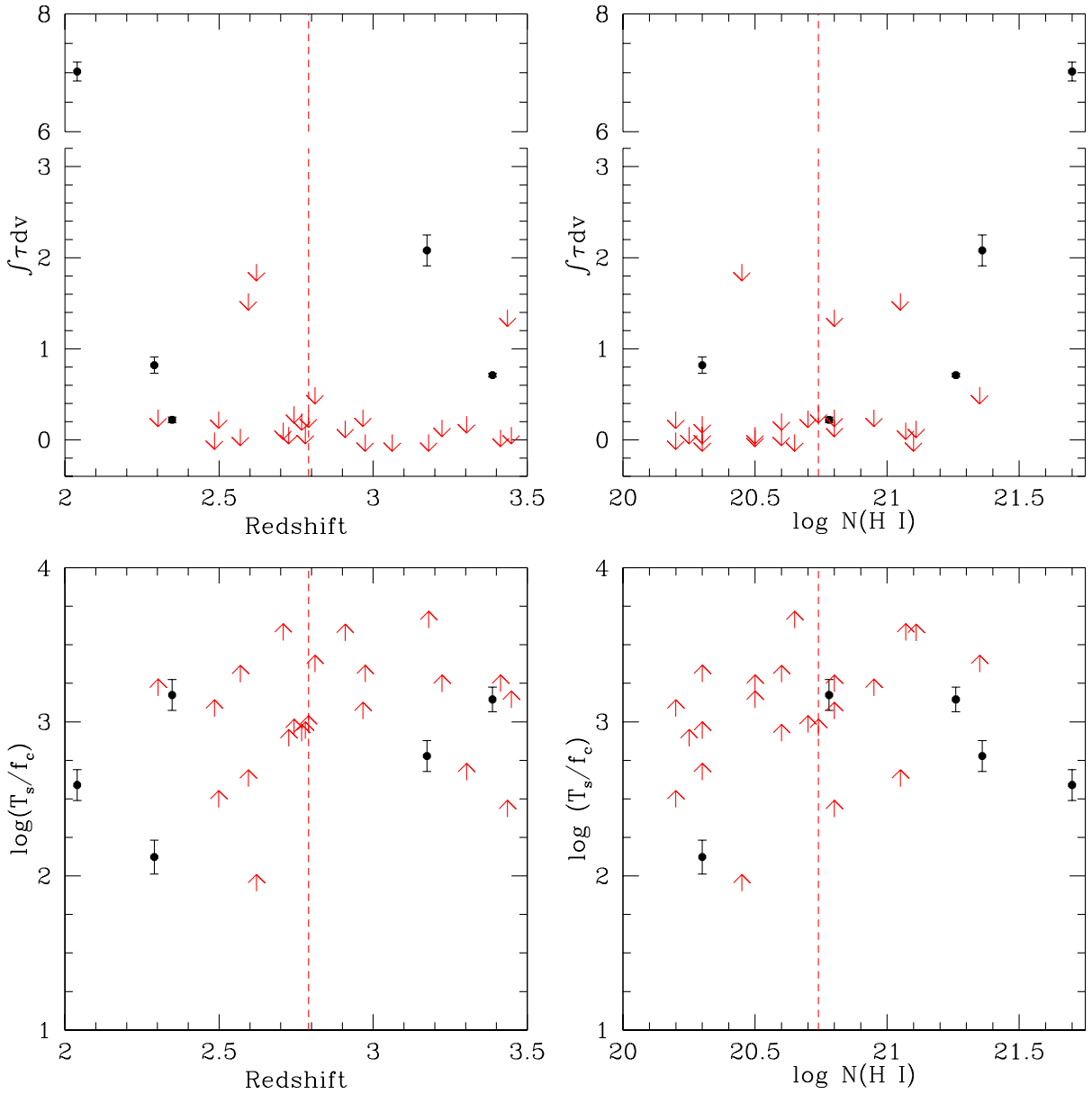

Figure 6. Properties of 21-cm absorptions vs redshift and N(H I). The vertical dashed lines give the median value of the quantity plotted in the x-axis.

Mg II systems at $1.10 \leq z \leq 1.45$ (see also Kanekar et al. 2009).

5.2 Redshift dependence

In the left hand side panels of Fig. 6 we plot T_s/f_c and integrated 21-cm optical depth vs redshift. No clear correlation is evident in this figure. The non-parametric Kendall test finds no significant correlation between $\int \tau dv$ (or T_S) and z. Note our sample probes only a restricted redshift range in terms of time interval probed. However, the lack of correlation found here is consistent with the near constancy of T_s/f_c as a function of redshift found by Curran et al. (2010). Understanding the redshift dependence of T_S is very important in particular to address whether there is any evolution in T_s (Kanekar & Chengalur 2003) or geometric effects (Curran & Webb 2006). To make an unbiased comparison we need to have 21-cm measurements at low z for a well defined sample of DLAs detected based on Lyα absorption.

5.3 Dependence on N(H I)

Recently Curran et al. (2010) have found a 3σ level correlation between N(H I) and T_s/f_c. To check whether this correlation holds at $z > 2$, we plot, in the top panels of Fig. 6, the integrated 21-cm optical depth as a function of redshift and N(H I). We note that there is a tendency for more 21-cm detections in DLAs with higher N(H I). However, the non-parametric Kendall test finds no significant correlation between $\int \tau dv$ and N(H I). In the bottom right

panel we plot T_S/f_c against log N(H I). The Kendall test does not show any significant relation between the two quantities (1.28σ with a probability of 0.2 for this to be due to chance). Thus we do not find any evidence for the 21-cm optical depth to depend on N(H I) in our sample.

6 21-CM ABSORPTION AND H_2

As 21-cm absorption and H_2 molecules can give complementary information on the physical state of the gas. In this Section, we study the relationship between these two indicators. There are 13 DLAs in our extended sample for which the expected optical wavelength range of redshifted H_2 absorptions has been observed at high spectral resolution. Nine of these sources are part of the UVES sample of Noterdaeme et al. (2008). Srianand et al. (2010) have reported the detection of H_2 in J1337+3152 and here we report the search for H_2 in the remaining three DLAs (z_{abs}= 3.3871 towards J0203+1134, z_{abs}= 2.7799 towards J1357−1744 and z_{abs}= 2.9091 towards J2344+3433). In the 10th column of Table 6, we summarize the molecular fraction $f(H_2) = 2N(H_2)/(2N(H_2)+N(H\ I))$] derived for these 13 systems.

In 8 systems, neither 21-cm absorption nor H_2 molecules are detected with typical upper limits of the order of 10^{-6} for $f(H_2)$. Apart from the system at $z_{abs} = 2.6214$ towards J0407−4410, the lower limits on T_S/f_c for the remaining 7 systems are higher than 700 K. There are 4 cases where f_c measurements are available. In three cases ($z_{abs} = 3.1799$ towards J0337−1204, $z_{abs} = 3.0619$ towards J0339−0133 and $z_{abs} = 2.9019$ towards J2344+3433), the lower limit on T_S is more than 2000 K. These are in line with the suggestion by Petitjean et al. (2000) that the absence of H_2 in most of the DLAs is due to the low density and high temperature of the gas.

In two cases ($z_{abs} = 2.5947$ towards J0407−4410 (CTS 247) and $z_{abs} = 2.8112$ towards J0530−2503 (PKS 0528-250)), strong H_2 absorption is detected with rotational excitations consistent with the H_2-bearing gas being a CNM. However, 21-cm absorption is not detected in either case. We discuss these two systems in detail below.

Among the five 21-cm absorbers, high resolution UVES spectra covering the expected wavelength range of H_2 absorption are available for four systems. The exception is the $z_{abs} = 2.28977$ system towards J0314+4314 (B0311+430). For the $z_{abs} = 2.3474$ system towards J0440−4333 (B0438−436) the continuum flux in the expected wavelength range is removed by high ionization lines from an associated system, as well as by a high-z Lyman limit system present along the line of sight. Below we discuss the five systems where simultaneous analysis of H_2 and 21-cm absorption is possible.

6.1 z_{abs}= 3.3868 DLA towards J0203+1134 (PKS 0201+113)

Searches for 21-cm absorption in this system have yielded conflicting results (de Bruyn et al. 1996; Briggs et al. 1997). Based on GMRT spectra taken at three different epochs, Kanekar et al. (2007) reported the detection of 21-cm absorption in two components at $z_{abs} = 3.387144(17)$ and 3.386141(45). Using N(H I)$\sim (1.8\pm0.3)\times10^{21}$ cm^{-2} they obtained $T_S = [955 \pm 160](f_c/0.69)$ K. Using high resolution optical spectrum, Ellison et al. (2001) have found a gas phase metallicity of 1/20 of solar with very little dust depletion. The gas cooling rate, log $l_c = -26.67 \pm 0.10$ erg s^{-1} Hz^{-1}, derived using C II* absorption is consistent with this DLA being part of high-cool population defined by Wolfe et al. (2003). From Kanekar et al. (2007) we can see that the strongest 21-cm absorption does not correspond to the strongest velocity component in either C II* or Fe II.

Here we report the detection of H_2 absorption from J=0 and J=1 levels originating from both Lyman and Werner bands (see Fig. 7). A single component Voigt profile fit reproduces the data well. As the Lyman-α forest is dense and the spectral signal-to-noise ratio is not very high due to the faintness of the QSO, we considered a range of b values (i.e between 1 and 5 km s^{-1}) to get the best fit values of log[$N(H_2$, J=0)] in the range 16.10−14.48 and log[$N(H_2$, J=1)] = 16.03−14.57. We estimated the kinetic temperature using the ortho-to-para ratio (i.e T_{01}) and found it to be in the range 48−108 K for the range of b parameters considered above. We note that for b parameters greater than 2 km s^{-1}, the H_2 lines are mainly in the linear portion of the curve of growth and the column density estimate is insensitive to the assumed value. The average molecular fraction, $log\ f(H_2)$, in the range, $-4.6 \leq log\ f(H_2) \leq -6.2$.

Despite the gas being cold, there is no 21-cm absorption detected at the position of the H_2 component (at z = 3.38679) which is well separated from the 21-cm absorption components If we use $f_c = 0.76$, as found by Kanekar et al. (2009) using 326 MHz observations, we find log N(H I) $\leq$ 19.12. This is less than 1% of the total H I column density measured in this system.

Unlike most of the strong H_2 systems, this system does not show detectable C I absorption. This means we do not have, unfortunately, an independent estimate of the density from fine-structure excitation.

6.2 z_{abs}= 2.5948 towards J0407-4410 (CTS 247)

As the radio source is faint, our GBT spectrum only gives a weak limit on the spin temperature, $T_S \geq 380$ K when we use a line width of 10 km s^{-1}. Srianand et al. (2005) have reported log N(C II*) = 13.66±0.13. This, together with log N(H I) = 21.05±0.10, gives a gas cooling rate of log $l_c = 26.92 \pm 0.16$. This is very close to the value l_c^{crit} that seems to demarcate between the high and low cool systems defined by Wolfe et al. (2008).

Ledoux et al. (2003) reported the detection of H_2 from this system. The H_2 absorption is well fitted with two components at $z_{abs} = 2.59471$ and 2.49486 with log $N(H_2) = 18.14$ and 15.51 respectively (Srianand et al. 2005). These components have $T_{01} = 121\pm10$ and 91±6 K respectively. The average molecular fraction, log $f(H_2)$, is found to be $-2.42^{+0.07}_{-0.12}$ with an average metallicity of -1.02 ± 0.12 and moderate dust depletion (Ledoux et al. 2003).

The absence of 21-cm absorption from this system is intriguing as H_2 components have T$\sim$100 K. With the same b parameters as used to fit the H_2 lines and the rms from the GBT spectrum, we get a 3σ upper limit of $\int \tau dv =$ 0.88 km s^{-1}. This translates to a constraint, $f_c \times N$(H I) $\leq$

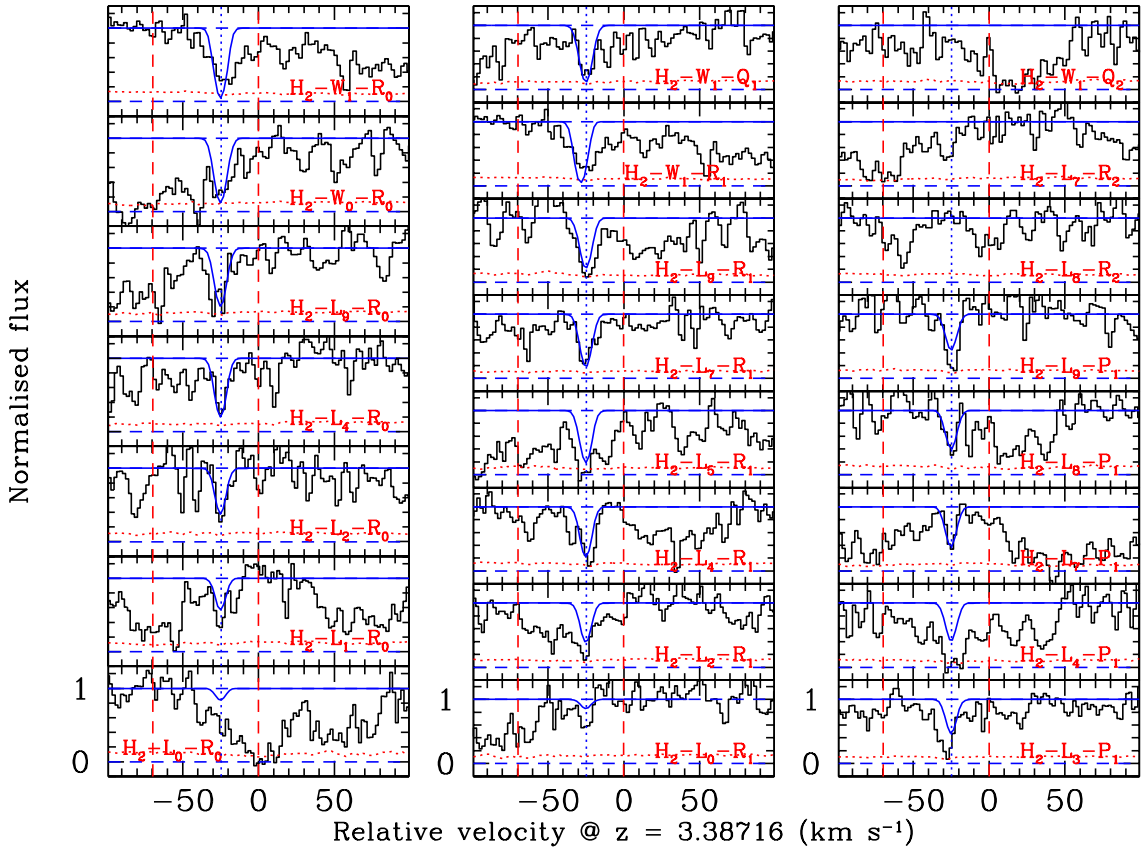

Figure 7. Voigt profile fits to H_2 Lyman and Werner band absorption lines in the z_{abs} = 3.3868 DLA system towards J0203+1134 (PKS 0201+113). The zero of the velocity scale is defined at z = 3.38716. The two vertical lines at v = 0 and −68 km s^{-1} show the locations of two 21-cm absorption components reported by (Kanekar et al. 2007). The vertical dotted line indicates the location of H_2 absorption. In each panel we also show the error spectrum with dotted curves.

2×10^{20} cm^{-2} in the H_2 components where we have assumed $T_S = T_{01}$. Unfortunately we do not have a VLBA image of this source and it is difficult to constrain the covering factor of the gas. If we assume $f_c \sim 1$ then the upper limit on N(H I) implies that the H_2 component is a sub-DLA with log $f(H_2) > -1.85$.

From the column densities of the C I fine-structure lines, Srianand et al. (2005) have constrained the particle density in the gas to be in the range $4.5 < n_H(cm^{-3}) < 57.3$. For $n_H = 4.5$ cm^{-3} and $f_c = 1$, we estimate the thickness of the H_2 cloud (i.e N(H I)/n_H) along the line of sight to be ≤ 15 pc.

6.3 z_{abs}= 2.0395 towards J0501−0159 (B0458-020)

21-cm absorption in two velocity components was reported by Wolfe et al. (1985). The background radio source shows structure over a wide range of scales and the absorbing cloud seems to cover most of these components (Briggs et al. 1989). The estimated extent of the H I absorber is ∼8 kpc and the spin-temperature of the system is 390 K.

C II* absorption is detected and the measured cooling rate is $l_c = -26.41 \pm 0.10$ (Wolfe et al. 2008). This is consistent with the high cool population. H_2 molecules are not detected with an upper limit of the molecular fraction of log $f(H_2) \leq -6.52$. This is one of the rare DLAs to show Lyman-α emission in the middle of the DLA absorption (Møller et al. 2004; Heinmüller et al. 2006).

Based on the star formation rate derived from the Lyman-α flux, Heinmüller et al. (2006) argued that the ambient radiation field is 10 times higher than the Galactic UV background. This excess radiation could be the main reason for the absence of H_2 in the gas. This picture is also confirmed by the lack of associated C I absorption.

6.4 z_{abs}= 2.8111 towards J0530-2503 (PKS 0528−250)

Carilli et al. (1996) searched for 21-cm absorption in this system using the WSRT and did not find any significant absorption. Recently Curran et al. (2010) have reported GBT observations of this source with a better signal-to-noise. They obtain a lower limit of the spin temperature of 700 K for $f_c = 1$, again assuming a width of 10 km s^{-1}. This source was found to be compact in the low frequency VLBA images with $f_c = 0.94$ (Kanekar et al. 2009).

No measurement of cooling rate is possible for this sys-

tem as the the C II* absorption is blended with other saturated lines.

This system has log N(H I) = 21.35±0.07, $Z = -0.91 \pm 0.07$ and $z_{\rm abs}$ higher than $z_{\rm em}$. This is the first high redshift DLA where H_2 absorption has been detected (Levshakov & Varshalovich 1985; Srianand & Petitjean 1998; Srianand et al. 2005). The high resolution UVES spectrum reveals two strong H_2 components at $z_{\rm abs} = 2.81100$ and 2.81112 with log $N(H_2) = 17.93^{+0.14}_{-0.20}$ and $17.90^{+0.11}_{-0.14}$, and $T_{01} = 167\pm7$ and 138±12 K respectively.

We re-reduced the GBT data of Curran et al. (2010) in the same way as our GBT data and found the rms in the frequency range expected for the 21-cm absorption associated with the H_2 components to be 6.7 mJy. This, together with the temperature T_{01} and the H_2 b parameter give a constraint of log N(H I) ≤ 20 in the H_2 components.

C I absorption is detected only in one of the H_2 components (i.e at $z_{\rm abs} = 2.81112$)(Srianand et al. 2005). From the C I level populations and for the above temperature, we derive that the particle density is in the range $25 < n_{\rm H}({\rm cm}^{-3}) < 270$. If we use the N(H I) limit of 10^{20} cm^{-2} derived from the 21-cm absorption, and use the constraint we get for the hydrogen density in the case of the $z_{\rm abs}$= 2.81112 component, we get a limit on the thickness of the gas along the line of sight to be 1.33 pc.

6.5 $z_{\rm abs}$= 3.1745 towards J1337+3152

Detection of 21-cm and H_2 in this system was reported in Srianand et al. (2010). The weak H_2 absorption is well aligned with the strongest metal line component but is slightly shifted by 2.5 km s^{-1}with respect to the 21-cm absorption component. This again suggests that the two transitions do not originate exactly from the same gas and that the absorptions arise from an inhomogeneous absorbing region.

As the H_2 column density is very low and the ratio of $N(H_2,J=0)$ to $N(H_2,J=1)$ is close to the maximum value allowed by the Boltzmann distribution, we cannot constrain the kinetic temperature of the gas. C II* absorption is detected with a total column density log N(C II*) = 13.61±0.08. Using log N(H I) = 21.36±0.10 we derive a gas cooling rate of log $l_{\rm c} = -27.28 \pm 0.13$. Thus the system belongs to the low cool part of the DLA population. The quasar is unresolved in our 1420 MHz VLBA image with a total flux density consistent with the measurement from FIRST observations. This suggests that most of the emission is in the unresolved component. Using Gaussian fits we estimate the limit on the largest angular size to be ≤ 3.8 mas (or ≤ 30 pc at $z_{\rm abs}$). Given the compact nature of the radio source it is intriguing to see the difference between the H_2 and 21-cm absorptions. This clearly shows that the absorbing gas contains a mixture of different phases at parsec scales.

7 RESULTS AND DISCUSSION

We have carried out a systematic search for 21-cm absorption in 10 DLAs at $z_{\rm abs}$> 2 using GMRT and GBT. We detect 21-cm absorption in only one of them. From our sample we find the 21-cm detection rate is 13% for a $\int \tau dv$ limit of 0.4 km/s (the detection limit reached in the case of J1337+3152). We also obtained 1420 MHz VLBI images for the sources in our sample.

The 21-cm detection at $z \geq 2$ seems to favour systems with high metallicity and/or high N(H I) (see also Kanekar et al. 2009; Curran et al. 2010). This basically means that the probability of detecting cold components that can produce detectable 21-cm absorption is higher in systems with high values of N(H I) and Z. However, we do not find any correlation between the integrated optical depth (or $T_{\rm S}/f_{\rm c}$) and N(H I) or metallicity.

It is important to address the covering factor issue before drawing any conclusions on T_S. Ideally one should do high spatial resolution VLBA spectroscopy for this purpose (see for example Lane et al. 2000). However, this is not possible at present specially for $z \geq 2$ absorbers. Therefore, we proceed by assuming that the core fraction found in the VLBA images as the covering factor of the absorbing gas (as in the case of Kanekar et al. 2009). We find that more than 50% of DLAs have weighted mean spin temperature ($T_{\rm S}$) in excess of 700 K. For the assumed temperature of the CNM gas $T_{\rm S}^{C} = 200$ K (as seen in H_2 components in high-z DLAs) we find that more than 73% of H I in such systems is originating from WNM. The median value CNM fraction (i.e f(CNM)) obtained for the detections and the median value of upper limits in the case of non-detections are in the range 0.2 to 0.25.

We study the connection between 21-cm and H_2 absorption in a sub-sample of 13 DLAs where both these species can be searched for. We report the detection and detailed analysis of H_2 molecules in the $z_{\rm abs}$=3.3871 DLA system towards J0203+1134 where 21-cm absorption is also detected. For a b parameter in the range 1-5 km s^{-1} we find 14.57≤log $N(H_2)$≤16.03. The inferred kinetic temperature is in the range 48-108 K based on T_{01} of H_2. However no 21-cm absorption is detected at the very position of this H_2 component. This suggests that the H I column density associated with this component is ≤ 10^{19} cm^{-2}. However, the lack of proper coincidence between 21-cm and any of the strong UV absorption components may also mean that the radio and optical sight lines probe different volumes of the gas.

In the case of 8 DLAs, neither 21-cm nor H_2 are detected. Typical upper limits on the molecular fraction (f_{H_2}) in these systems are ≤ 10^{-6}. The lack of H_2 in DLAs can be explained if the H I gas originates from low density regions photoionized by the metagalactic UV (see for example, Petitjean et al. 1992, 2000; Hirashita & Ferrara 2005). This also indicates that the volume filling factor of H_2 in DLAs is small (Zwaan & Prochaska 2006). Typical limits obtained for $T_{\rm S}$ in these systems are consistent with only a small fraction of the H I gas originating from the CNM phase as suggested by the lack of H_2 absorption.

In two cases strong H_2 absorption is detected and kinetic temperatures are in the range 100-200 K, but 21-cm absorption is not detected. Even in two cases where both the species are detected they do not originate from the same velocity component. The lack of 21-cm absorption directly associated with H_2 indicates that only a small fraction (typically ≤ 10%) of the neutral hydrogen seen in the DLA is associated with the H_2 components (see also

Noterdaeme et al. 2010). This implies that the molecular fractions $f(H_2)$ reported from the H_2 surveys should be considered as conservative lower limits for the H_2 components.

For two of the H_2-bearing DLAs with density measurements based on C I fine-structure excitation we derive an upper limit on the line of sight thickness of ≤ 15 pc. This is consistent with the size estimate for the H_2-bearing gas in $z_{\rm abs}$= 2.2377 DLA towards Q1232+082 based on partial coverage (Balashev et al. 2011).

In principle, the presence of H_2 and 21-cm absorptions in a single component provides a unique combination to simultaneously constrain the variation of the fine-structure constant (α), the electron-to-proton mass ratio (μ) and the proton G-factor. As shown here, DLAs with 21-cm and H_2 detections are rare. Even in these cases the presence of multiphase structure at parsec scale is evident, introducing velocity shifts between the different absorption components that will affect the constraints on the variation of constants.

8 ACKNOWLEDGEMENTS

We thank GBT, GMRT, VLBA and VLT staff for their support during the observations and the anonymous referee for some useful comments. We acknowledge the use of SDSS spectra from the archive (http://www.sdss.org/). The National Radio Astronomy Observatory is a facility of the National Science Foundation operated under cooperative agreement by Associated Universities, Inc. VLBA data were correlated using NRAO's implementation of the DiFX software correlator that was developed as part of the Australian Major National Research Facilities Programme and operated under licence. RS and PPJ gratefully acknowledge support from the Indo-French Centre for the Promotion of Advanced Research (Centre Franco-Indien pour la promotion de la recherche avancée) under Project N.4304-2.

REFERENCES

Akerman C. J., Ellison S. L., Pettini M., Steidel C. C., 2005, A&A, 440, 499
Balashev S. A., Petitjean P., Ivanchik A. V., Ledoux C., Srianand R., Noterdaeme P., Varshalovich D. A., 2011, MNRAS, pp 1400–+
Briggs F. H., Brinks E., Wolfe A. M., 1997, AJ, 113, 467
Briggs F. H., Wolfe A. M., Liszt H. S., Davis M. M., Turner K. L., 1989, ApJ, 341, 650
Carilli C. L., Lane W., de Bruyn A. G., Braun R., Miley G. K., 1996, AJ, 111, 1830
Curran S. J., Tzanavaris P., Darling J. K., Whiting M. T., Webb J. K., Bignell C., Athreya R., Murphy M. T., 2010, MNRAS, 402, 35
Curran S. J., Tzanavaris P., Pihlström Y. M., Webb J. K., 2007, MNRAS, 382, 1331
Curran S. J., Webb J. K., 2006, MNRAS, 371, 356
de Avillez M. A., Breitschwerdt D., 2004, A&A, 425, 899
de Bruyn A. G., O'Dea C. P., Baum S. A., 1996, A&A, 305, 450
Ellison S. L., Pettini M., Steidel C. C., Shapley A. E., 2001, ApJ, 549, 770
Ellison S. L., York B. A., Pettini M., Kanekar N., 2008, MNRAS, 388, 1349
Gupta N., Salter C. J., Saikia D. J., Ghosh T., Jeyakumar S., 2006, MNRAS, 373, 972
Gupta N., Srianand R., Petitjean P., Noterdaeme P., Saikia D. J., 2009, MNRAS, 398, 201
Heinmüller J., Petitjean P., Ledoux C., Caucci S., Srianand R., 2006, A&A, 449, 33
Hirashita H., Ferrara A., 2005, MNRAS, 356, 1529
Isobe T., Feigelson E. D., Nelson P. I., 1986, ApJ, 306, 490
Kanekar N., Chengalur J. N., 2003, A&A, 399, 857
Kanekar N., Chengalur J. N., Lane W. M., 2007, MNRAS, 375, 1528
Kanekar N., Lane W. M., Momjian E., Briggs F. H., Chengalur J. N., 2009, MNRAS, 394, L61
Kanekar N., Prochaska J. X., Ellison S. L., Chengalur J. N., 2009, MNRAS, 396, 385
Kanekar N., Smette A., Briggs F. H., Chengalur J. N., 2009, ApJ, 705, L40
Kanekar N., Subrahmanyan R., Ellison S. L., Lane W. M., Chengalur J. N., 2006, MNRAS, 370, L46
Kulkarni S. R., Heiles C., 1988, Neutral hydrogen and the diffuse interstellar medium. pp 95–153
Lane W. M., Briggs F. H., Smette A., 2000, ApJ, 532, 146
Ledoux C., Petitjean P., Srianand R., 2003, MNRAS, 346, 209
Levshakov S. A., Varshalovich D. A., 1985, MNRAS, 212, 517
Møller P., Fynbo J. P. U., Fall S. M., 2004, A&A, 422, L33
Noterdaeme P., Ledoux C., Petitjean P., Srianand R., 2008, A&A, 481, 327
Noterdaeme P., Ledoux C., Srianand R., Petitjean P., Lopez S., 2009, A&A, 503, 765
Noterdaeme P., Petitjean P., Ledoux C., López S., Srianand R., Vergani S. D., 2010, A&A, 523, A80+
Noterdaeme P., Petitjean P., Ledoux C., Srianand R., 2009, A&A, 505, 1087
Noterdaeme P., Petitjean P., Srianand R., Ledoux C., López S., 2011, A&A, 526, L7+
Petitjean P., Bergeron J., Puget J. L., 1992, A&A, 265, 375
Petitjean P., Ledoux C., Noterdaeme P., Srianand R., 2006, A&A, 456, L9
Petitjean P., Srianand R., Ledoux C., 2000, A&A, 364, L26
Prochaska J. X., Herbert-Fort S., Wolfe A. M., 2005, ApJ, 635, 123
Srianand R., Gupta N., Petitjean P., Noterdaeme P., Ledoux C., 2010, MNRAS, 405, 1888
Srianand R., Noterdaeme P., Ledoux C., Petitjean P., 2008, A&A, 482, L39
Srianand R., Petitjean P., 1998, A&A, 335, 33
Srianand R., Petitjean P., Ledoux C., Ferland G., Shaw G., 2005, MNRAS, 362, 549
Wolfe A. M., Briggs F. H., Turnshek D. A., Davis M. M., Smith H. E., Cohen R. D., 1985, ApJ, 294, L67
Wolfe A. M., Gawiser E., Prochaska J. X., 2003, ApJ, 593, 235
Wolfe A. M., Gawiser E., Prochaska J. X., 2005, ARA&A, 43, 861
Wolfe A. M., Prochaska J. X., Gawiser E., 2003, ApJ, 593, 215
Wolfe A. M., Prochaska J. X., Jorgenson R. A., Rafelski M., 2008, ApJ, 681, 881

Wolfire M. G., Hollenbach D., McKee C. F., Tielens A. G. G. M., Bakes E. L. O., 1995, ApJ, 443, 152
York B. A., Kanekar N., Ellison S. L., Pettini M., 2007, MNRAS, 382, L53
Zwaan M. A., Prochaska J. X., 2006, ApJ, 643, 675